PHYSICAL REVIEW B **94**, 060101(R) (2016)

Characterization of hyperfine interaction between an NV electron spin and a first-shell ^{13}C nuclear spin in diamond

K. Rama Koteswara Rao and Dieter Suter
Fakultät Physik, Technische Universität Dortmund, D-44221, Germany
(Received 3 March 2016; published 3 August 2016)

The nitrogen-vacancy (NV) center in diamond has attractive properties for a number of quantum technologies that rely on the spin angular momentum of the electron and the nuclei adjacent to the center. The nucleus with the strongest interaction is the ^{13}C nuclear spin of the first shell. Using this degree of freedom effectively hinges on precise data on the hyperfine interaction between the electronic and the nuclear spin. Here, we present detailed experimental data on this interaction, together with an analysis that yields all parameters of the hyperfine tensor, as well as its orientation with respect to the atomic structure of the center.

DOI: 10.1103/PhysRevB.94.060101

Nitrogen-vacancy (NV) centers in diamond have interesting properties for applications in room-temperature metrology, spectroscopy, and quantum information processing (QIP) [1–6]. Nuclear spins, coupled by hyperfine interaction to the electron spin of the NV center, are important for many of these applications [1,3,6–13]. For example, in QIP applications, the nuclear spins can hold quantum information [12,13], serving as part of a quantum register [1]. Accurate knowledge of the hyperfine interaction is necessary, e.g., for designing precise and fast control sequences for the nuclear spins [14,15]. With a known Hamiltonian, control sequences can be tailored by optimal control techniques to dramatically improve the speed and precision of multiqubit gates [16–19].

The ^{13}C nuclear spin of the first coordination shell is a good choice for a qubit due to its large hyperfine coupling to the electronic spin of the NV center, which can be used to implement fast gate operations [3,20,21] or high-speed quantum memories [22]. Full exploitation of this potential requires accurate knowledge of the hyperfine interaction, including the anisotropic (tensor) components. The interaction tensor has been calculated by density functional theory (DFT) [23–26], but only a limited number of experimental studies of this hyperfine interaction exist to date [27–29]. In this work, we present a detailed analysis of this hyperfine interaction. The experiments were carried out on a single NV center of a diamond crystal with a natural abundance of ^{13}C and a nitrogen concentration of <5 ppb using a home-built confocal microscope and microwave electronics for excitation [22]. This center is located at a depth of ≈8 μm from the surface of the diamond.

The presence of a nuclear spin in the first coordination shell reduces the symmetry of the NV center from C_{3V} to C_S, a single mirror plane. This symmetry plane passes through the NV symmetry axis and the ^{13}C nuclear spin as illustrated in Fig. 1(a). The NV symmetry axis defines the z axis of the NV frame of reference, the x axis lies in the symmetry plane of the center, and the y axis is perpendicular to both of them. Due to the symmetry of the system, only those elements of the hyperfine tensor that are invariant with respect to the inversion of the y coordinate can be nonzero. Hence, the Hamiltonian of the hyperfine interaction between the electron spin ($S = 1$) and the ^{13}C nuclear spin ($I = 1/2$) of the first shell can be written in the NV frame of reference as

$$\mathcal{H}_{\rm hf} = A_{zz}S_zI_z + A_{xx}S_xI_x + A_{yy}S_yI_y + A_{xz}(S_xI_z + S_zI_x). \tag{1}$$

Here, S_α and I_α represent components of the electron and nuclear spin angular momenta, respectively, and $A_{\alpha\beta}$ represents the components of the hyperfine tensor. The full Hamiltonian of the system consisting of an NV electron spin and a ^{13}C nuclear spin can be written as

$$\mathcal{H} = DS_z^2 + \gamma_e\mathbf{B}\cdot\mathbf{S} + \gamma_n\mathbf{B}\cdot\mathbf{I} + \mathcal{H}_{\rm hf}. \tag{2}$$

Here, D represents the zero-field splitting of the electron spin, γ_e and γ_n are the gyromagnetic ratios of the electron and nuclear spins respectively, $\mathbf{B} = B(\sin\theta\cos\phi,\ \sin\theta\sin\phi,\ \cos\theta)$ represents the magnetic field vector, and θ and ϕ represent its polar and azimuthal angles in the NV frame of reference. For typical magnetic fields, the nuclear Zeeman interaction is much smaller than the other components of the Hamiltonian and the quantization axis of the nuclear spin is dominated by the hyperfine interaction. In the present analysis, we ignore the hyperfine interaction of the ^{14}N nuclear spin, which is small compared to the hyperfine interaction under investigation. Figure 1(b) shows the energy level diagram of the system. There are eight possible transitions of the electron spin from the two $m_S = 0$ states to the four $m_S = \pm1$ states. The first two of these transitions are shown by red arrows, while the green wave marks the nuclear spin transition within the $m_S = 0$ multiplet. Figure 1(c) shows a typical experimental electron spin resonance (ESR) spectrum containing 24 resonance lines. The additional factor of 3 is due to the hyperfine interaction with the ^{14}N nuclear spin, which we neglect in the present context.

We start the determination of the hyperfine tensor by measuring ESR spectra for different orientations of the magnetic field vector and then fitting the resonance frequencies to obtain all relevant Hamiltonian parameters, including the orientation of the NV center with respect to the laboratory frame. As a first step we determined the orientation of the NV axis of the center, which corresponds to the z axis of the Hamiltonian of Eq. (2). For this purpose, we rotated the magnetic field with a fixed magnitude around two orthogonal rotation axes crossing at the NV center [29]. ESR spectra were measured as Fourier transforms of Ramsey fringes for nine noncoplanar orientations of the magnetic field [30]. The transition frequencies of these spectra were fitted numerically to determine the orientation of the z axis of the center. This orientation was reconfirmed by also measuring spectra of a neighboring NV center with no ^{13}C nucleus in the

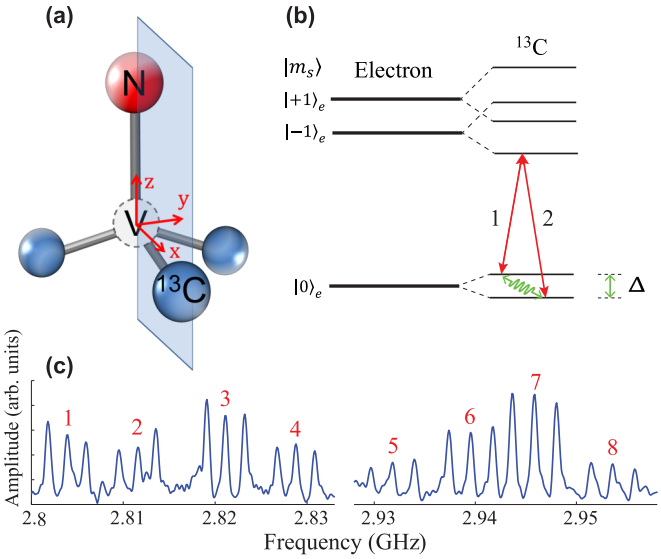

FIG. 1. Symmetry of the system along with the energy level diagram and spectra. (a) Structure of the NV center in diamond with a first shell ^{13}C. The mirror plane and the x, y, and z axes of the NV frame are also shown. (b) Energy level diagram considering only the electron and ^{13}C nuclear spins. The red arrows and green wave represent electron and nuclear spin transitions, respectively. (c) Experimental ESR spectrum for a particular orientation of the magnetic field vector. The spectrum consists of 24 resonance lines due to the interaction with the ^{14}N nuclear spin.

first coordination shell. The two data sets yielded the same direction for the z axis. If the field is aligned with the z axis, the splitting between the transitions $m_s = 0 \leftrightarrow m_s = \pm 1$ reaches a maximum. The numerical fit also provided estimates of the Hamiltonian parameters $D \approx 2870.2$ (± 1.3) MHz, $\gamma_e B \approx 63.3$ (± 0.8) MHz, and $\sqrt{A_{zz}^2 + A_{xz}^2} \approx 131.2$ (± 1.1) MHz, which give the dominant contribution to the transition frequencies when $\mathbf{B}||z$.

The A_{xx} and A_{yy} components of the hyperfine tensor contribute only in second order to the energies and spectral positions. Accordingly, their uncertainty is quite large. Their influence on the transition frequencies is maximized if the magnetic field is close to the xy plane. The highest precision is obtained by measuring the transitions with the smallest linewidth. In the NV system, this is the nuclear spin transition between the $m_S = 0, m_I = \pm 1/2$ states. As a nuclear spin transition, the width of this resonance line is about one order of magnitude smaller (≈60 kHz) than that of the ESR transitions. This transition can be excited not only by resonant radio-frequency pulses, but also by the Raman excitation scheme shown in Fig. 1(b): A microwave pulse that drives the transitions from both $|m_S = 0, m_I = \pm 1/2\rangle$ states to one of the $m_S = \pm 1$ states creates nuclear spin coherence and can also probe this nuclear spin coherence by converting it back into population of the $m_S = 0$ state [30]. The optimal duration of the microwave excitation pulse for the nuclear spin coherence is in general twice as long as that of the optimal pulse for the ESR transitions. Apart from the narrower linewidth, the nuclear spin transition can be identified in the ESR spectrum as a zero-quantum transition: Its position does not change with the carrier frequency used for the excitation and readout pulses.

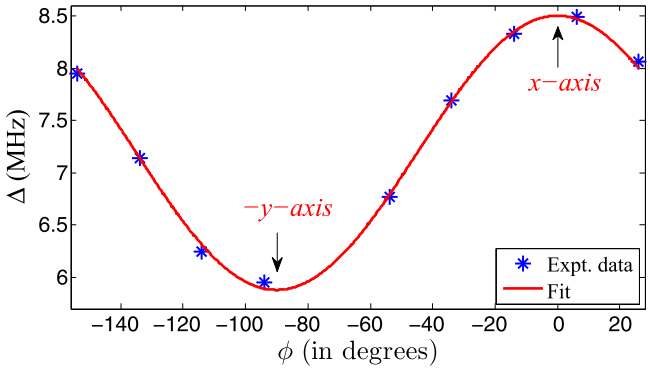

FIG. 2. Zero-quantum transition frequencies for an azimuthal (ϕ) rotation of the magnetic field for $\theta = 84.5°$. The experimental data (blue stars) were fitted to the equation $\kappa_1 \cos^2\phi + \kappa_2 \sin^2\phi$. The fit parameters are $\kappa_1 = 8.5$ MHz and $\kappa_2 = 5.88$ MHz.

Using second-order perturbation theory, its frequency can be written as [29]

$$\Delta \approx \frac{2|\gamma_e B \sin\theta|}{D}\left(\sqrt{A_{xx}^2 + A_{xz}^2}\cos^2\phi + |A_{yy}|\sin^2\phi\right). \quad (3)$$

Therefore, by measuring these zero-quantum frequencies for different orientations of the magnetic field for a fixed angle θ, it is possible to obtain estimates of the quantities $\sqrt{(A_{xx}^2 + A_{xz}^2)}$ and $|A_{yy}|$. Figure 2 shows a graphical representation of the experimental data, measured for magnetic fields oriented at an angle $\theta = 84.5°$ from the z axis, together with the numerical fit.

From the fitted curve, we find that the parameters $\sqrt{(A_{xx}^2 + A_{xz}^2)}$ and $|A_{yy}|$ must have the values ≈193.0 (± 1.5) and 133.5 (± 1.9) MHz. The quantity $\sqrt{(A_{xx}^2 + A_{xz}^2)}$ is larger (smaller) than $|A_{yy}|$ if the maximum (minimum) of the zero-quantum frequencies corresponds to the x axis. Combining these data with those for $D, \sqrt{(A_{zz}^2 + A_{xz}^2)}$, and $\gamma_e B$, we obtain several possible parameter sets, with different signs, two different orientations for the x and y axes, and different ratios A_{xz}/A_{zz}.

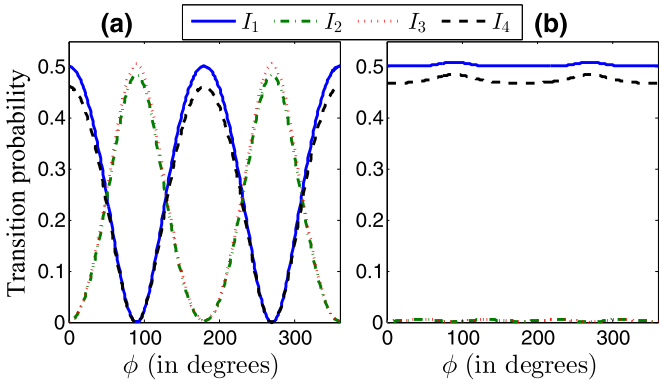

FIG. 3. Transition probabilities of low-frequency ESR lines ($\nu < 2870$ MHz) when $\mathbf{B}$ is oriented in the xy plane. Panel (a) corresponds to the sign combinations of the hyperfine parameters such that $\det(A) > 0$, and for panel (b), $\det(A) < 0$.

To eliminate the remaining ambiguities and to determine the orientation of the x and y axes, it is important to use not only the transition frequencies, but also the transition amplitudes (dipole moments). For this purpose, we measured the transition amplitudes of the spectral lines for different orientations of the magnetic field. The experimental amplitudes depend also on the orientation of the microwave magnetic field. Since absolute amplitudes are hard to measure, we determined ratios of transitions amplitudes for two different data sets: First, we measured ratios of Rabi frequencies for pairs of transitions whose frequencies differ by the nuclear spin transition frequency discussed above [30]. These transitions connect the two $m_S = 0$ states with the same $m_S = \pm 1$ state. In the second set of data, we compared the transition amplitudes of spectra for different orientations of the magnetic field in the xy plane. The first set of data indicated that the x axis corresponds to the maximum of the zero-quantum frequency (see Fig. 2). This implies that $\sqrt{(A_{xx}^2 + A_{xz}^2)} \approx 193.0\ (\pm 1.5)$ MHz and $|A_{yy}| \approx 133.5\ (\pm 1.9)$ MHz. These data also indicate that if A_{xx} and A_{zz} have the same sign, the ratio $|A_{xz}/A_{zz}|$ must be < 0.3.

Figure 3 shows the numerically calculated transition probabilities of the low-frequency spectral lines ($\nu < 2870$ MHz) as a function of the azimuthal angle ϕ of the magnetic field in the xy plane. For the calculation, the microwave field was chosen to be along the x axis of the NV frame of reference. Here, we observe two qualitatively different cases, depending on the relative signs of the hyperfine parameters. Labeling the transition probabilities in ascending frequency order as $I_1 \ldots I_4$, we observe strong variations when $\det(A) > 0$, with I_1 and I_4 in phase and I_2, I_3 shifted by 90°. However, for $\det(A) < 0$, the amplitudes are almost constant, with I_2 and I_3 much smaller than I_1 and I_4. In Fig. 4, we compare the experimental ratios of amplitudes of spectral lines with the corresponding ratios of simulated transition probabilities. The simulation has a good match with the experimental data, if we choose $\det(A) > 0$ for the hyperfine parameters and the transverse component of the microwave field is at an angle of 103° from the x axis of the NV frame. The maximum of the quantity $(I_1 + I_4)/(I_2 + I_3)$ is much higher in the simulation compared to the experimental data. This can be attributed to the limited signal-to-noise ratio of the experimental spectra and the off-resonance effects of the microwave pulses. Small errors ($\approx 1°$) in the orientation of the magnetic field can also contribute to this deviation. In any case, the experimental data make it clear that each of the quantities $(I_1 + I_4)/(I_2 + I_3)$ and $(I_2 + I_3)/(I_1 + I_4)$ is higher than the other for different values of ϕ, which excludes the case $\det(A) < 0$ as for this one, the quantity $(I_2 + I_3)/(I_1 + I_4)$ is always higher than the quantity $(I_1 + I_4)/(I_2 + I_3)$. Therefore, we disregard the parameter sets with $\det(A) < 0$ in the following.

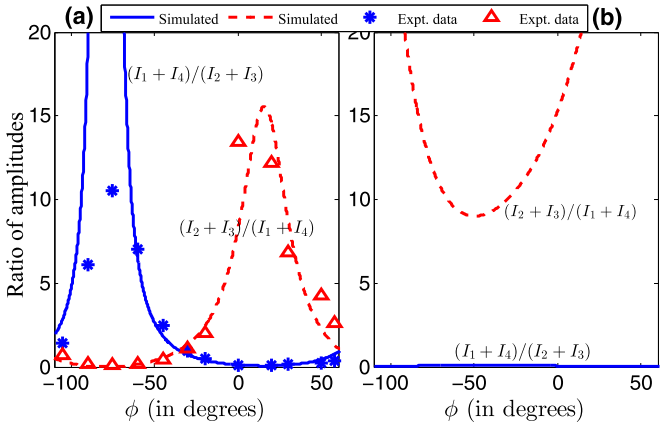

FIG. 4. Ratios of amplitudes of the low-frequency spectral lines ($\nu < 2870$ MHz) as a function of ϕ of the magnetic field in the xy plane. The experimental data (blue stars and red triangles) are compared to the simulated ones (blue solid and red dashed lines). Panel (a) corresponds to $\det(A) > 0$, and for panel (b), $\det(A) < 0$.

From a combined fit of the available experimental data, we thus obtained values for all components of the hyperfine tensor. Table I lists the different parameter sets, in the NV frame of reference, that are compatible with the experimental data. The signs of A_{xz} can be chosen positive or negative; the sign change corresponds to a π rotation around the z axis.

It is useful to consider also the principal axis representation of the hyperfine tensor, which can be obtained by diagonalizing the hyperfine matrix of the NV frame of reference (Table I). We write $\overline{A}_{xx}$, $\overline{A}_{yy}$, and $\overline{A}_{zz}$ for the principal components of the hyperfine tensor in increasing magnitude. Table II lists the possible values for the principal components. All four solutions have the same principal components, except for the signs. These solutions result in identical transition frequencies and amplitudes and are therefore experimentally indistinguishable. The y axes of the principal axis system (PAS) and the NV frame of reference coincide and the angle between the NV symmetry axis and the z axis of the PAS is $\zeta = 109.3°$. As a second-rank tensor, the hyperfine tensor is invariant under π rotations around the principal axes. Accordingly, orientations with the angles $-\zeta$ and $180° \pm \zeta$ are equivalent solutions. All of these solutions are compatible with the experimental data. Since DFT calculations [24,31] indicate that the largest component of the hyperfine tensor, which we write as $\overline{A}_{zz}$, points in the direction of the ^{13}C atom, the solution $\zeta = 109.3°$ appears to be the most meaningful one, since it agrees very well with the theoretical value 109.5° obtained from the geometry.

The hyperfine tensor components determined here are in reasonable agreement with other values found in the literature.

TABLE I. Hyperfine tensor components in the NV frame of reference.

Sol. #	1	2	3	4
A_{xx} (MHz)	189.3 (±1.1)	−189.3 (±1.1)	−163.0 (±2.4)	163.0 (±2.4)
A_{yy} (MHz)	128.4 (±1.0)	128.4 (±1.0)	−128.4 (±1.0)	−128.4 (±1.0)
A_{zz} (MHz)	128.9 (±4.3)	−128.9 (±4.3)	85.7 (±3.3)	−85.7 (±3.3)
A_{xz} (MHz)	±24.1 (±1.2)	∓24.1 (±1.2)	∓99.3 (±2.8)	±99.3 (±2.8)

TABLE II. Hyperfine tensor components in its PAS.

Sol. #	1	2	3	4
$\overline{A}_{xx}$ (MHz)	120.5 (±3.9)	−120.5 (±3.9)	−120.5 (±3.4)	120.5 (±3.4)
$\overline{A}_{yy}$ (MHz)	128.4 (±1.0)	128.4 (±1.0)	−128.4 (±1.0)	−128.4 (±1.0)
$\overline{A}_{zz}$ (MHz)	197.8 (±1.3)	−197.8 (±1.3)	197.8 (±2.8)	−197.8 (±2.8)

The values from the earlier ensemble EPR measurements [28,31] are $\overline{A}_{\parallel} = \overline{A}_{zz} = 199.7$ and $\overline{A}_{\perp} = \sqrt{\overline{A}_{xx}^2 + \overline{A}_{yy}^2} = 120.3$ MHz, and those from the DFT calculations [24,26] are $\overline{A}_{xx} = 114.0$, $\overline{A}_{yy} = 114.1$, and $\overline{A}_{zz} = 198.4$ MHz. However, the earlier experimental studies assumed uniaxial symmetry of the hyperfine tensor and there was no information about the signs of the hyperfine components. Here, we measured the deviation from the uniaxial symmetry and found four equivalent sign combinations.

The parameter set determined in Ref. [29], which was given as $A_{xx} = 166.9$, $A_{yy} = 122.9$, $A_{zz} = 90.0$, and $A_{xz} = -90.3$ MHz in the NV frame of reference, is comparable in magnitude with solutions 3 and 4 of Table I. However, the signs of the parameters and the ratio $|A_{xz}/A_{zz}|$ together are not compatible with the measured ratios of Rabi frequencies of ESR transitions as discussed earlier.

In conclusion, we have performed a detailed analysis of the hyperfine interaction between an NV electron spin and a ^{13}C nuclear spin of the first shell. This analysis yielded accurately the hyperfine tensor and its PAS. The present study will be helpful in implementing precise control operations in quantum registers containing the first-shell ^{13}C nuclear spin of the NV center. This nuclear spin is particularly attractive because of its strong coupling to the NV electron spin, which is necessary for implementing fast gate operations in hybrid quantum registers consisting of electron and nuclear spins.

We gratefully acknowledge experimental assistance from J. Zhang and useful discussions with F. D. Brandão, J. H. Shim, and T. S. Mahesh. This work was supported by the DFG through Grant No. Su 192/31-1.

[1] M. V. G. Dutt, L. Childress, L. Jiang, E. Togan, J. Maze, F. Jelezko, A. S. Zibrov, P. R. Hemmer, and M. D. Lukin, Science **316**, 1312 (2007).

[2] G. Balasubramanian, I. Chan, R. Kolesov, M. Al-Hmoud, J. Tisler, C. Shin, C. Kim, A. Wojcik, P. R. Hemmer, A. Krueger *et al.*, Nature (London) **455**, 648 (2008).

[3] P. Neumann, N. Mizuochi, F. Rempp, P. Hemmer, H. Watanabe, S. Yamasaki, V. Jacques, T. Gaebel, F. Jelezko, and J. Wrachtrup, Science **320**, 1326 (2008).

[4] F. Dolde, H. Fedder, M. W. Doherty, T. Nbauer, F. Rempp, G. Balasubramanian, T. Wolf, F. Reinhard, L. Hollenberg, F. Jelezko *et al.*, Nat. Phys. **7**, 459 (2011).

[5] T. Staudacher, F. Shi, S. Pezzagna, J. Meijer, J. Du, C. A. Meriles, F. Reinhard, and J. Wrachtrup, Science **339**, 561 (2013).

[6] G. Waldherr, Y. Wang, S. Zaiser, M. Jamali, T. Schulte-Herbrüggen, H. Abe, T. Ohshima, J. Isoya, J. Du, P. Neumann *et al.*, Nature (London) **506**, 204 (2014).

[7] L. Childress, M. V. Gurudev Dutt, J. M. Taylor, A. S. Zibrov, F. Jelezko, J. Wrachtrup, P. R. Hemmer, and M. D. Lukin, Science **314**, 281 (2006).

[8] P. Neumann, J. Beck, M. Steiner, F. Rempp, H. Fedder, P. R. Hemmer, J. Wrachtrup, and F. Jelezko, Science **329**, 542 (2010).

[9] B. Smeltzer, L. Childress, and A. Gali, New J. Phys. **13**, 025021 (2011).

[10] T. H. Taminiau, J. Cramer, T. van der Sar, V. V. Dobrovitski, and R. Hanson, Nat. Nanotechnol. **9**, 171 (2014).

[11] G. A. Álvarez, C. O. Bretschneider, R. Fischer, P. London, H. Kanda, S. Onoda, J. Isoya, D. Gershoni, and L. Frydman, Nat. Commun. **6**, 8456 (2015).

[12] G. Fuchs, G. Burkard, P. Klimov, and D. Awschalom, Nat. Phys. **7**, 789 (2011).

[13] P. C. Maurer, G. Kucsko, C. Latta, L. Jiang, N. Y. Yao, S. D. Bennett, F. Pastawski, D. Hunger, N. Chisholm, M. Markham, D. J. Twitchen, J. I. Cirac, and M. D. Lukin, Science **336**, 1283 (2012).

[14] B. Smeltzer, J. McIntyre, and L. Childress, Phys. Rev. A **80**, 050302 (2009).

[15] M. Chen, M. Hirose, and P. Cappellaro, Phys. Rev. B **92**, 020101 (2015).

[16] N. Khaneja, T. Reiss, C. Kehlet, T. Schulte-Herbrggen, and S. J. Glaser, J. Magn. Reson. **172**, 296 (2005).

[17] N. Khaneja, Phys. Rev. A **76**, 032326 (2007).

[18] Y. Chou, S.-Y. Huang, and H.-S. Goan, Phys. Rev. A **91**, 052315 (2015).

[19] X. Rong, J. Geng, F. Shi, Y. Liu, K. Xu, W. Ma, F. Kong, Z. Jiang, Y. Wu, and J. Du, Nat. Commun. **6**, 8748 (2015).

[20] F. Jelezko, T. Gaebel, I. Popa, M. Domhan, A. Gruber, and J. Wrachtrup, Phys. Rev. Lett. **93**, 130501 (2004).

[21] N. Mizuochi, P. Neumann, F. Rempp, J. Beck, V. Jacques, P. Siyushev, K. Nakamura, D. J. Twitchen, H. Watanabe, S. Yamasaki, F. Jelezko, and J. Wrachtrup, Phys. Rev. B **80**, 041201 (2009).

[22] J. H. Shim, I. Niemeyer, J. Zhang, and D. Suter, Phys. Rev. A **87**, 012301 (2013).

[23] M. Łuszczek, R. Laskowski, and P. Horodecki, Physica B (Amsterdam, Neth.) **348**, 292 (2004).

[24] A. Gali, M. Fyta, and E. Kaxiras, Phys. Rev. B **77**, 155206 (2008).

[25] A. P. Nizovtsev, S. Y. Kilin, V. A. Pushkarchuk, A. L. Pushkarchuk, and S. A. Kuten, Opt. Spectrosc. (USSR) **108**, 230 (2010).

[26] K. Szász, T. Hornos, M. Marsman, and A. Gali, Phys. Rev. B **88**, 075202 (2013).

[27] J. H. N. Loubser and J. A. van Wyk, Rep. Prog. Phys. **41**, 1201 (1978).

[28] S. Felton, A. M. Edmonds, M. E. Newton, P. M. Martineau, D. Fisher, D. J. Twitchen, and J. M. Baker, Phys. Rev. B **79**, 075203 (2009).

[29] J. H. Shim, B. Nowak, I. Niemeyer, J. Zhang, F. D. Brandao, and D. Suter, arXiv:1307.0257.

[30] See Supplemental Material at http://link.aps.org/supplemental/10.1103/PhysRevB.94.060101 for the experimental pulse sequences, and example experimental data showing the electron and the nuclear spin transitions and the selective Rabi oscillations of the electron spin transitions.

[31] M. Simanovskaia, K. Jensen, A. Jarmola, K. Aulenbacher, N. Manson, and D. Budker, Phys. Rev. B **87**, 224106 (2013).